Journal of Materials Chemistry B

ROYAL SOCIETY OF CHEMISTRY

PAPER

View Article Online
View Journal | View Issue

Cite this: J. Mater. Chem. B, 2025, 13, 10960

Theoretical insights into adhesion mechanisms of dental adhesives on zirconia surfaces: effects of functional groups in adhesive monomers

Yosuke Sumiya *[a] and Takahiro Uwabe[b]

Received 24th May 2025,
Accepted 25th July 2025

DOI: 10.1039/d5tb01248a

rsc.li/materials-b

This study investigates the adhesion mechanism of dental adhesives to zirconia (ZrO_2) using periodic density functional theory (DFT). ZrO_2 is extensively used as a prosthetic material. Dental adhesives for ZrO_2 typically contain adhesive monomers such as 10-methacryloyloxydecyl dihydrogen phosphate (10-MDP) or 2-(methacryloxy)ethyl phenyl hydrogen phosphate (2-MEP), 2-(methacryloxy)ethyl phenyl hydrogen phosphate (Phenyl-P), and 4-methacryloxyethyl trimellitic acid (4-MET). This study investigates the effects of acidic functional groups, including phosphoric acid, phenyl phosphate, and phthalate, on adhesion. For all adhesive monomers on clean zirconia surfaces, no barrier proton transfer from the acidic functional group to the surface occurred, and a minimal difference in adhesive strength was detected. In contrast, on the hydroxylated surface, only the phosphate group contained in 2-MEP caused proton transfer, resulting in higher adhesive strength. After releasing a proton, the oxygen atom served as a hydrogen-bond acceptor, forming interfacial interactions involving charge transfer. This proton transfer was attributed to the high acidity of the phosphoric acid group. These results provide insights into the molecular mechanisms governing adhesion of zirconia dental materials.

1. Introduction

Adhesive technology is essential in modern dentistry, significantly advancing innovations in clinical techniques. Adhesion to prosthetic materials is a key factor in the long-term maintenance of prosthetic materials and the quality of treatment.[1] Recently, the widespread adoption of computer-aided design/computer aided-manufacturing (CAD/CAM) systems[2] has facilitated the extensive use of zirconia (ZrO_2) as a prosthetic material.[3,4] ZrO_2 exhibits excellent mechanical strength, biocompatibility, and esthetics[5–7] and is often used in dental applications as a yttria-stabilized tetragonal ZrO_2 polycrystal (Y-TZP).[8] However, tetragonal zirconia (t-ZrO_2) exhibits low chemical activity and it remains a challenge to ensure strong and long-term adhesion.

Adhesive monomers such as 10-methacryloyloxydecyl dihydrogen phosphate (10-MDP), 2-(methacryloxy)ethyl phenyl hydrogen phosphate (Phenyl-P), and 4-methacryloxyethyl trimellitic acid (4-MET) have been widely used, each containing an acidic functional group. These monomers are classified as self-etching adhesives, enabling simultaneous conditioning and priming of the substrates without the need for a separate etching process.[9,10] The adhesive properties of 10-MDP, Phenyl-P, and 4-MET are attributed to phosphate, phenyl phosphate, and carboxylic acid groups, respectively. Each structure of the monomers is shown in Fig. 1. An alternative to 10-MDP is 2-(methacryloxy)ethyl phenyl hydrogen phosphate (2-MEP), differing in carbon chain length (Fig. 1(a)). Although the adhesion mechanisms of these adhesives to dentin[11] and 10-MDP to zirconia[12,13] have been analyzed experimentally, a comprehensive understanding of their adhesion to zirconia remains limited.[14] This knowledge gap primarily arises from the difficulty in directly observing the adhesive layer, which is buried by the constituent materials,[15] and a detailed analysis of its interfacial interactions remains challenging. Hence, a detailed theoretical investigation of the effects of different adhesive monomers on the interactions with zirconia surfaces at the molecular level is essential.

Computational techniques such as density functional theory (DFT) calculations and molecular dynamics (MD) simulations are effective in investigating the adhesion mechanisms. These approaches have been extensively used to analyze adhesive interactions in industrial materials[16–32] and hold promise for applications in dental adhesion interfaces. Our recent work has just revealed the effects of various zirconia crystals on the adhesive mechanism.[33] In this study, the interfacial interactions were analyzed using DFT calculations to theoretically

[a] Department of Applied Chemistry, Yamaguchi University, 2-16-1 Tokiwadai, Ube, Yamaguchi, 755-8611, Japan. E-mail: yosuke.sumiya@yamaguchi-u.ac.jp
[b] Institute for Materials Chemistry and Engineering and IRCCS, Kyushu University, Nishi-Ku, Fukuoka 819-0395, Japan

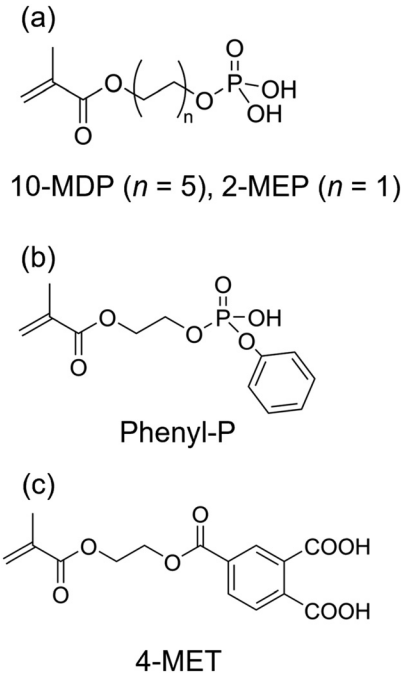

Fig. 1 Three adhesive monomers. (a) Phosphate monomers, n = 5 and 1, are referred to as 10-methacryloyloxydecyl dihydrogen phosphate (10-MDP) and 2-(methacryloxy)ethyl phenyl hydrogen phosphate (2-MEP), respectively, (b) 2-(methacryloxy)ethyl phenyl hydrogen phosphate (Phenyl-P) and (c) 4-methacryloxyethyl trimellitic acid (4-MET).

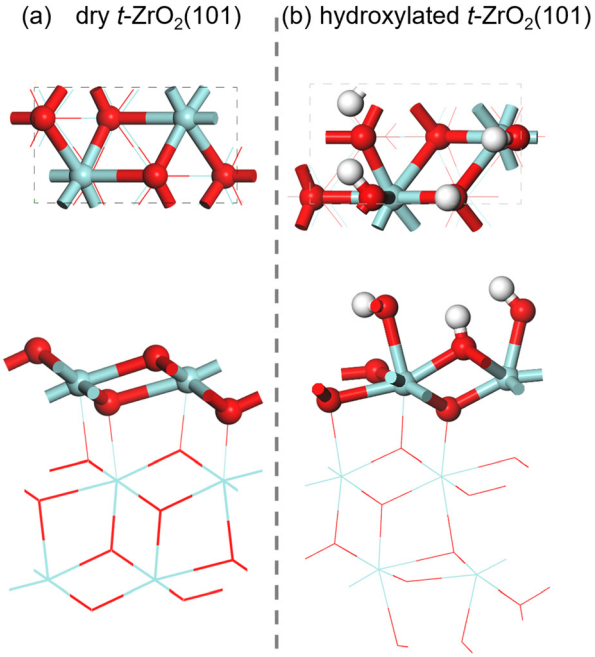

Fig. 2 Top and side views of unit cells of t-ZrO_2(101). (a) Dry and (b) hydroxylated surfaces; fixed atoms in density functional theory (DFT) optimization are drawn as thin lines.

elucidate the molecular adhesion mechanisms of the monomers—2-MEP, Phenyl-P, and 4-MET—on zirconia surfaces, with a specific focus on the role of acidic functional groups in adhesion. Since the carbon chain length in 2-MEP is less than that in 10-MDP, 2-MEP was used to efficiently analyze the various interactions. The findings offer valuable guidance for optimizing dental adhesive formulations. They also contribute to developing more effective bonding strategies for zirconia-based restorations.

2. Methodology

2.1. Modeling of ZrO_2 surfaces

To create the surface structure of t-ZrO_2, its crystal structure[34] was initially optimized using DFT calculations. The energetically most stable (101) surface[35,36] was then cut out and a vacuum layer of approximately 23 Å was added. This (101) surface was reported experimentally to be easily exposed.[37] This structure was optimized using DFT calculations to create a surface-slab model by relaxing only the first layer of the surface and fixing the lower layers, as shown in Fig. 2(a). In addition, considering the wet environment of the oral cavity, a hydroxylated surface model of chemisorbed water molecules was created, as shown in Fig. 2(b). The hydroxylated surface model was obtained by coordinating hydroxy groups on all zirconium atoms in the top and bottom layers of the clean surface. Hydrogen atoms were also added to the adjacent oxygen atoms. During this process, one hydrogen atom was transferred to the OH group to form a water molecule.

DFT calculations under periodic condition were performed using the Vienna Ab initio Simulation Package (VASP) 5.4.4.[38–40] The Perdew–Burke–Ernzerhof (PBE) form of the generalized gradient approximation (GGA) was used as the exchange–correlation functional.[41] Dispersion interactions were accounted for using the Grimme D3BJ method.[42] The electron–ion interactions were treated with the projector augmented wave (PAW) method.[43,44] Computational parameters were set as follows: a cutoff energy of the plane-wave basis set of 500 eV, a k-point mesh spacing of $2\pi \times 0.05$ Å^{-1}, a self-consistent field (SCF) convergence criterion of 1.0×10^{-5} eV, and an atomic force threshold of 0.03 eV Å^{-1}.

2.2. Modeling of adhesive/ZrO_2 surface complexes

To investigate the stable conformations of each adhesive conformer on the t-ZrO_2 surface, initial structures of the adhesive monomer were randomly placed on the surface, and MD simulations were performed using the Forcite module of the Materials Studio software.[45] The unit cells of the clean and hydroxylated surfaces were prepared into 2 × 2 supercells to accommodate the adhesive molecules. To explore the large conformational space, MD simulations were performed in the NVT ensemble with a Nose–Hoover thermostat[46] at 500 K using the DREIDING force field.[47] The time step and time-evolution were 0.5 fs and 5.0 ns, respectively. All the atoms containing the t-ZrO_2 surface were fixed, and only the adhesive molecules were relaxed. Snapshots were obtained every 50 ps during the MD simulation. From the resulting 100 structures, 10 energetically

stable structures were selected. These selected structures were then subjected to DFT optimizations, enabling the relaxation of the topmost layer of the surface and adhesive molecules, while the others remained fixed. The most stable structures were adopted as complex models of the adhesive molecules and surfaces. Applying the above procedure to all the adhesive molecules yields **1**–**3** and **1w**–**3w**, as shown in Fig. 3 and 4, respectively. The numbers of atoms in these structures were 168, 178, 181, 264, 274, and 277, respectively.

The adhesive interface models constructed in this manner were minimal, enabling an efficient analysis of the interactions between the surface and adhesives. The effects of metastable conformations and interactions between the adhesive molecules were excluded from these models. Moreover, in a more realistic setting, such as the oral environment, factors such as physisorbed water layers on the zirconia surface, oral cavity contaminants, surface modifications induced by pretreatment, and trace yttrium content in zirconia could play important roles. Addressing these issues remains an avenue for future research.

Regarding surface pretreatment, the effects of sandblasted zirconia surfaces on the adhesion of 2-MEP have been discussed in our previous study.[33] In this work, we showed that the methacryloyl group, which is responsible for polymerization, undergoes structural deformation on the monoclinic surface exposed by sandblasting.[48,49] Since both Phenyl-P and 4-MET also contain a methacryloyl group, comparable analyses are required for these monomers as well. With respect to physisorbed water layers, it has been reported that such layers weaken the adhesion performance of industrial epoxy resins.[50] A similar negative impact is anticipated for dental adhesives. For yttria doping, yttria segregation could occur depending on the fabrication process of Y-TZP.[51] The effect of segregation on adhesion is unclear due to alterations in the active sites on the surface,[52] and further investigation is required.

2.3. Calculation of adhesive strength

The tensile adhesive strength was estimated by the derivative of the potential energy curve as the adhesive molecule dissociated perpendicularly from the surface. To obtain the potential energy curves for the six adhesive/t-ZrO_2 interfaces constructed in the above procedure, the adhesive molecules were dissociated incrementally from the surface up to 8.0 Å in 0.1 Å steps, resulting in 80 structures. Single-point energy calculations were performed for each structure, and the energy E was plotted with respect to the displacement Δr. The resulting curve was fitted to the Morse potential:

$$E = D(1 - e^{-a\Delta r})^2 \quad (1)$$

where D denotes the adhesive energy and a is a system-specific constant. The most stable position of the adhesive molecule on the surface is defined as $\Delta r = 0$. By taking the derivative of the fitted energy curve with respect to Δr, the adhesive force F was obtained:

$$F = \frac{dE}{d\Delta r} \quad (2)$$

The maximum value in the adhesive force–displacement (F–Δr) curve was estimated as the adhesive strength F_{ad}:

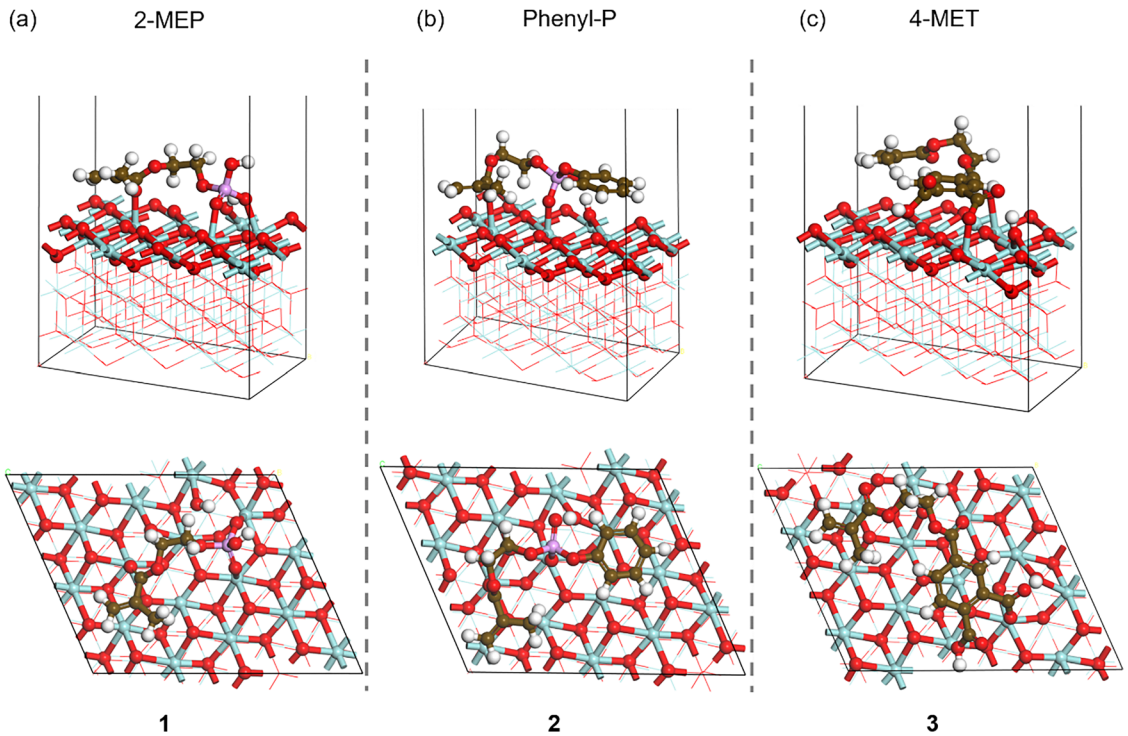

Fig. 3 Top views and overviews of the most stable structures of each adhesive molecule on the clean t-ZrO_2(101) surface: (a) 2-MEP, (b) Phenyl-P, and (c) 4-MET. Chemical bonds in low layers are drawn with fine lines.

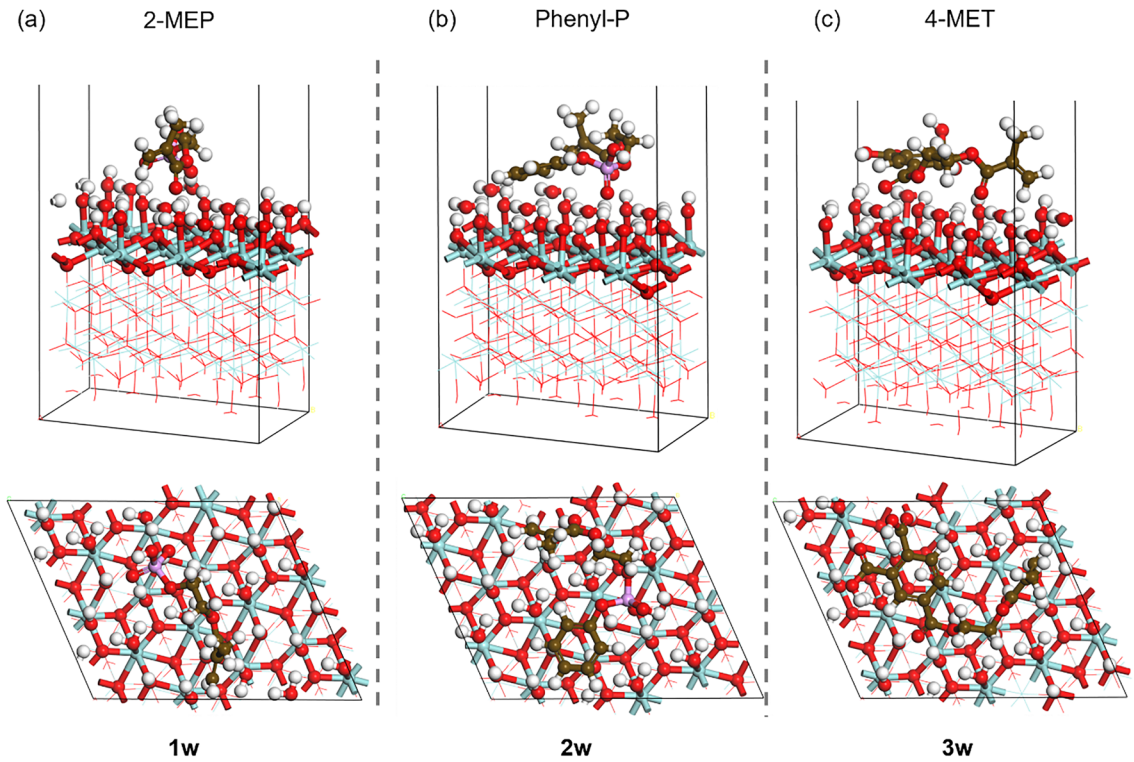

Fig. 4 Top views and overviews of the most stable structures of each adhesive molecule on the hydroxylated *t*-ZrO_2(101) surface: (a) 2-MEP, (b) Phenyl-P, and (c) 4-MET. Chemical bonds in low layers are drawn with fine lines.

$$F_{ad} = \max(F) \quad (3)$$

The total energy E can be decomposed into two components: the dispersion term and the remaining DFT term. This relationship was expressed as the sum of the dispersion energy $E_{dispersion}$ and DFT energy E_{DFT}:

$$E = E_{dispersion} + E_{DFT} \quad (4)$$

By differentiating both sides, the adhesive force F can also be decomposed into the dispersion and DFT forces ($F_{dispersion}$ and F_{DFT}).

$$F = F_{dispersion} + F_{DFT} \quad (5)$$

To evaluate these contributions, E_{DFT} was fitted to eqn (1). The derivative of the fitted curve with respect to the displacement yields F_{DFT}, and further subtraction from the total force F yields $F_{dispersion}$.

2.4. Visualization of interfacial interactions

Charge density difference calculations can be used to investigate the charge transfer interactions at adhesive interfaces.[53] The interactions between the adhesive molecule and the surface can be visualized using the difference in charge density before and after adhesion. The charge density difference is defined as follows:

$$\Delta\rho_{ad} = \rho_{complex} - (\rho_{surface} + \rho_{adhesive}) \quad (6)$$

where $\rho_{complex}$ represents the charge density of the system including the surface and the adhesive molecule, and $\rho_{surface}$ and $\rho_{adhesive}$ correspond to the charge densities of the isolated surface and the adhesive molecule, respectively. These individual charge densities were calculated separately, maintaining atomic positions identical to those in the complex.

To estimate the binding energies of interaction sites identified through charge density difference analysis, crystal orbital Hamilton population (COHP) calculations were used.[54] This analysis required projecting the plane wave functions onto a localized basis set, and this process was carried out using the local orbital basis suite towards electronic-structure reconstruction (LOBSTER) software.[55] Using the Hamiltonian matrix elements and crystal orbital expansion coefficients, the density of states (DOS) for a given atomic pair was separated into bonding and antibonding energy regions, yielding the projected COHP (pCOHP).[56] Bonding interactions correspond to negative values. The binding energy of an atomic pair is determined by integrating pCOHP up to the Fermi level E_F, producing the integrated crystal orbital Hamilton population (ICOHP), which is expressed as follows:[57]

$$\mathrm{ICOHP} = \int_{-\infty}^{E_F} \mathrm{pCOHP}(E)\mathrm{d}E \quad (7)$$

A more negative ICOHP value indicates a stronger bonding interaction, facilitating a comparison of the interaction strengths. In this study, we emphasize the distinction between DFT calculations and classical force-field methods: DFT

calculations enable the precise analysis of interactions involving charge transfer and chemical bond rearrangements that are difficult to simulate using a force-field-based approach.

3. Results and discussion

3.1 Energy and adhesive force curves of three adhesive monomers for the *t*-ZrO_2 surface

Fig. 5(a) shows the dissociation energy curves for the adhesive monomers in **1**, **2**, and **3**, as depicted in Fig. 3, on the clean *t*-ZrO_2 surface. Each energy curve exhibited a single inflection point, with the black, blue, and red curves corresponding to the **1**, **2**, and **3** energy curves, respectively, where the data points represent the computed values, and the solid lines represent the Morse potential fitting curves. The potential well depths, D, for these interactions were 7.0, 6.8, and 6.8 eV, respectively. As shown in Fig. 5(b), the estimated adhesive strengths (F_{ad}) of each adhesive molecule are nearly identical, 5.2, 5.5, and 5.6 nN for **1**–**3**, respectively. Adhesive force curves are shown in Fig. S1.

In contrast, Fig. 5(c) and (d) show that both the energy curves and adhesive strengths for the hydroxylated surface differ significantly from those of the clean surface. The D values for the hydroxylated interface **1w**–**3w** were 3.6, 1.7, and 1.9 eV, respectively, and F_{ad} values were 2.2, 1.4, and 1.6 nN, respectively. The adhesive strengths of all the adhesive molecules on the hydroxylated surface were reduced compared to those on the clean surface by 42%, 26%, and 30%, respectively. The F_{ad} value of **1w** was the highest, indicating that the decrease in adhesive strength owing to surface hydroxylation was most suppressed by 2-MEP. What causes the difference in adhesive strength on the hydroxylated surface? To clarify the origin, the energy and adhesive force curves are divided into DFT and dispersion contributions using eqn (4) and (5).

Fig. 6(a) and (b) show the maximum values of the F, F_{DFT}, and $F_{dispersion}$ curves for **1**–**3** and **1w**–**3w**, respectively. The black, red, and blue colors correspond to F, F_{DFT} and $F_{dispersion}$, respectively. The adhesive force curves are shown in Fig. S1. On the clean surface (**1**–**3**), the adhesive strengths of the DFT components were larger than those of the dispersion

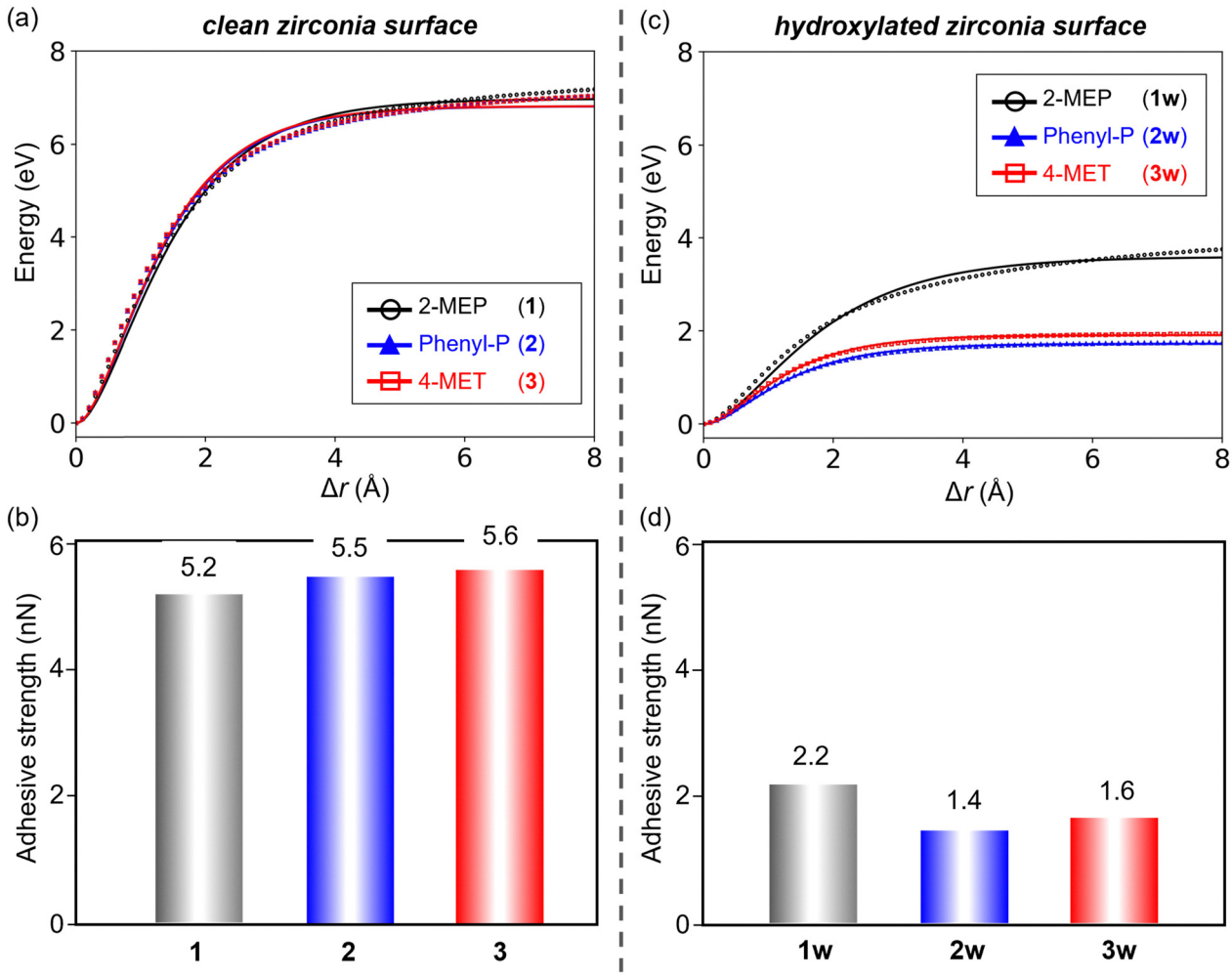

Fig. 5 (a) Energy curves and (b) adhesive strengths of three adhesive monomers for the clean *t*-ZrO_2(101) surface. (c) Energy curves and (d) adhesive strengths of three adhesive monomers for the hydroxylated *t*-ZrO_2(101) surface. Black, blue, and red colors correspond to 2-MEP, Phenyl-P, and 4-MET, respectively.

components. The adhesive strengths of the DFT components in **1**–**3** were 4.2, 4.1, and 3.9 nN, respectively, while those of the dispersion components were 1.1, 1.5, and 1.7 nN, respectively. The DFT component of **1** and the dispersion component of **3** were slightly larger, but not significant. In contrast, different trends were observed for the hydroxylated surfaces (**1w**–**3w**). The DFT component remains dominant for **1w**, whereas the dispersion component becomes dominant for **2w** and **3w**. The adhesive strengths of the DFT components of **1w**–**3w** were 1.6, 0.4, and 0.5 nN, respectively, while those of the dispersed components were 0.7, 1.0, and 1.1 nN, respectively. The order of the adhesive strengths of the DFT components corresponded to the order of F_{ad}. The difference in the DFT component of the adhesive strength between **1w** and the others (**2w** and **3w**) was larger than the corresponding difference in the dispersion component. This finding suggested that the difference in the adhesive strength of each structure was attributed to the DFT component. The interactions associated with the DFT

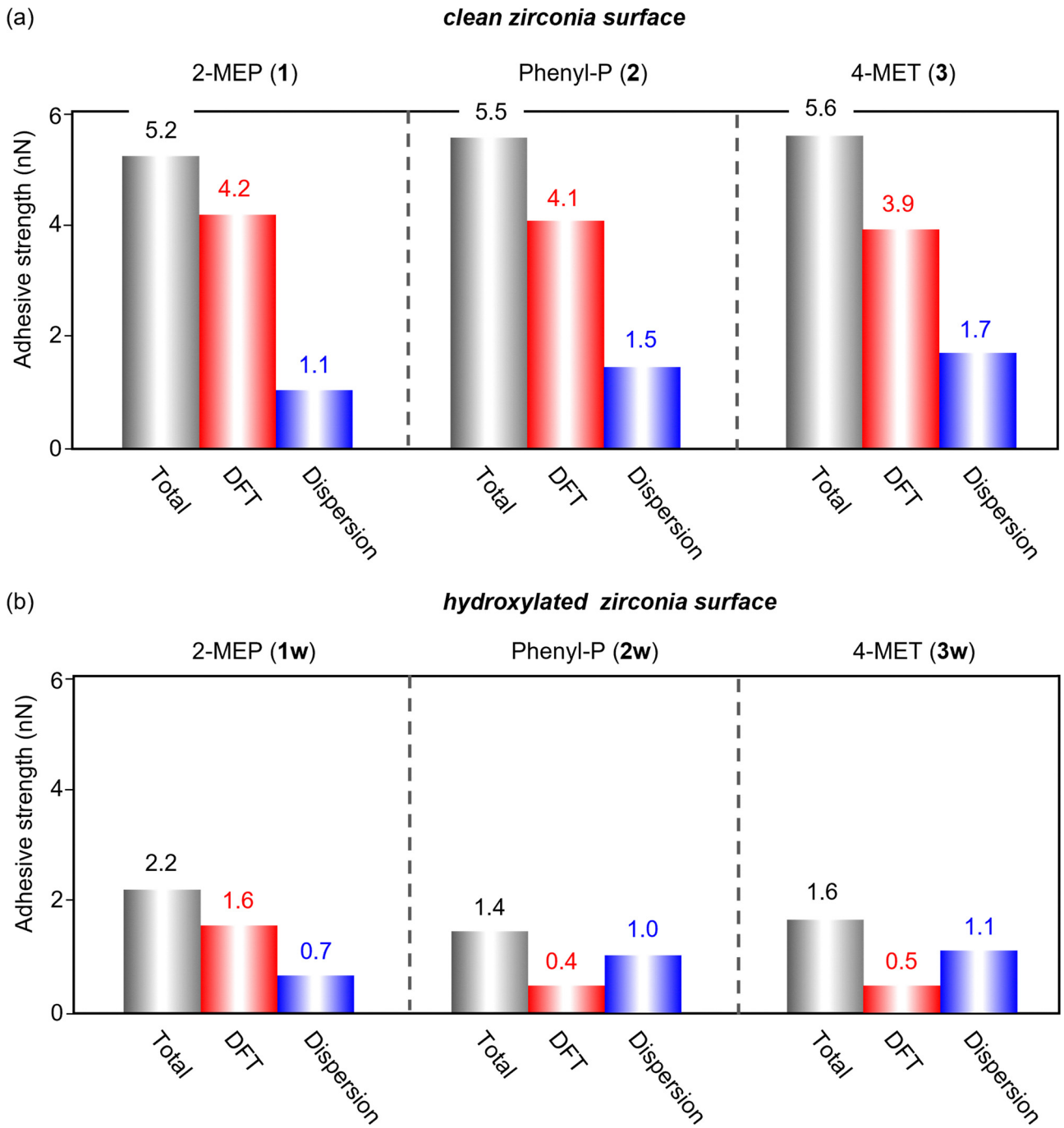

Fig. 6 Maximum values of DFT and dispersion components obtained by decomposition of the adhesive force curve. (a) and (b) Clean and hydroxylated *t*-ZrO_2(101) surfaces, respectively.

components involved charge transfer. In the next section, we visualize the interfacial interactions with charge transfer based on the charge density difference and discuss the differences in adhesion to clean and hydroxylated surfaces, as well as the factors contributing to the high adhesive strength of **1w**.

3.2. Adhesive interactions at the interfaces

To elucidate the effects of changes in molecular structure and charge density that contribute to differences in adhesion to clean and hydroxylated zirconia surfaces, charge density difference analysis was conducted for the **1–3** and **1w–3w** interfaces based on eqn (6). VESTA software[58] was used to visualize the structures. The charge density difference of **1** is shown in Fig. 7, whereas those of **2** and **3** are shown in Fig. 8. The interaction sites at each interface were visualized in these figures, with yellow and cyan representing charge accumulation and deficiency, respectively. For visibility, only the top surface layer was shown, with an isosurface value of 0.01 e $Å^{-3}$.

In Fig. 7(a), dotted lines (1) and (2) represent the sites where significant changes in the charge density are observed in **1**. These enlarged views from different angles are shown in Fig. 7(b), where the distances *d* of the interacting atomic pairs and their ICOHP values are detailed. In **1**, proton transfer from the phosphate group of 2-MEP to the surface occurred before and after DFT optimization, as shown in Fig. 7(c). After proton transfer, as labeled in (1A) and (1B), the two oxygen atoms of the phosphate group strongly interacted with the surface zirconium atoms, with their ICOHP values of −2.72 and −2.76 eV. Furthermore, the interaction between the oxygen atom and the hydrogen atom transferred to the surface after proton release was (1C), with an ICOHP value of −0.48 eV. The ICOHP value of interaction between the methacryloyl group and the zirconium atom referred as (2) was −2.76 eV. In this study, the adsorption structure was obtained by DFT optimization calculations, suggesting that proton transfer proceeds without energy barriers as 2-MEP approaches the clean zirconia surface.

In Fig. 8(a) and (d), the dotted lines indicate the sites for a significant change in charge density for **2** and **3**, respectively. The corresponding enlarged views from different angles are shown in Fig. 8(b) and (e). In **2** and **3**, proton transfer to the surface occurs as in **1**, and the structures highlighting these changes are shown in Fig. 8(c) and (f). In **2**, the oxygen atoms of the phenyl phosphate group interact strongly with the surface and are labeled as (1A) and (1B), respectively. These ICOHP values were −4.05 and −1.19 eV, respectively, and (1B) is the

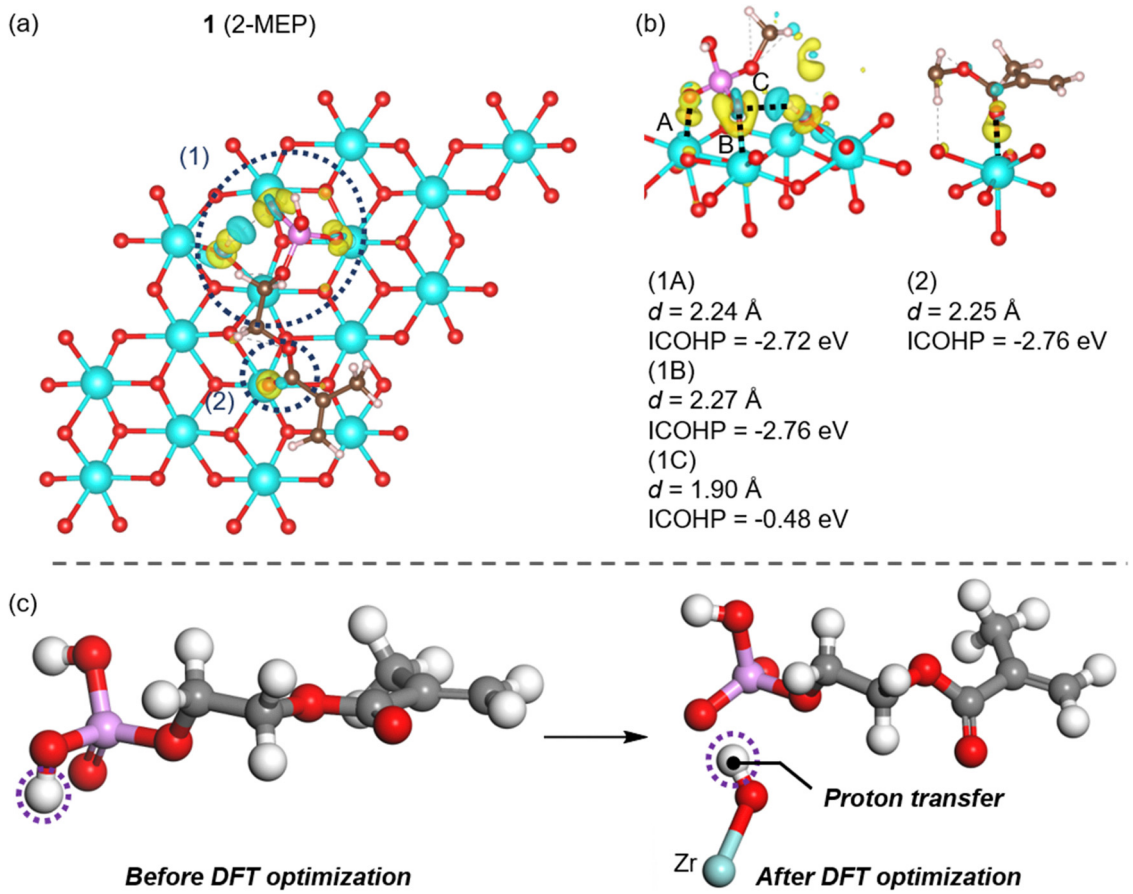

Fig. 7 (a) Charge density difference of **1**. (b) Enlarged views of sites (1) and (2) from different angles. Interatomic distances *d* and ICOHP values for the corresponding atomic pairs are shown. Interaction (1) is labelled as (1A), (1B), and (1C), respectively, as it involves three atomic pairs. (c) Structural change of 2-MEP in **1** *via* DFT optimization.

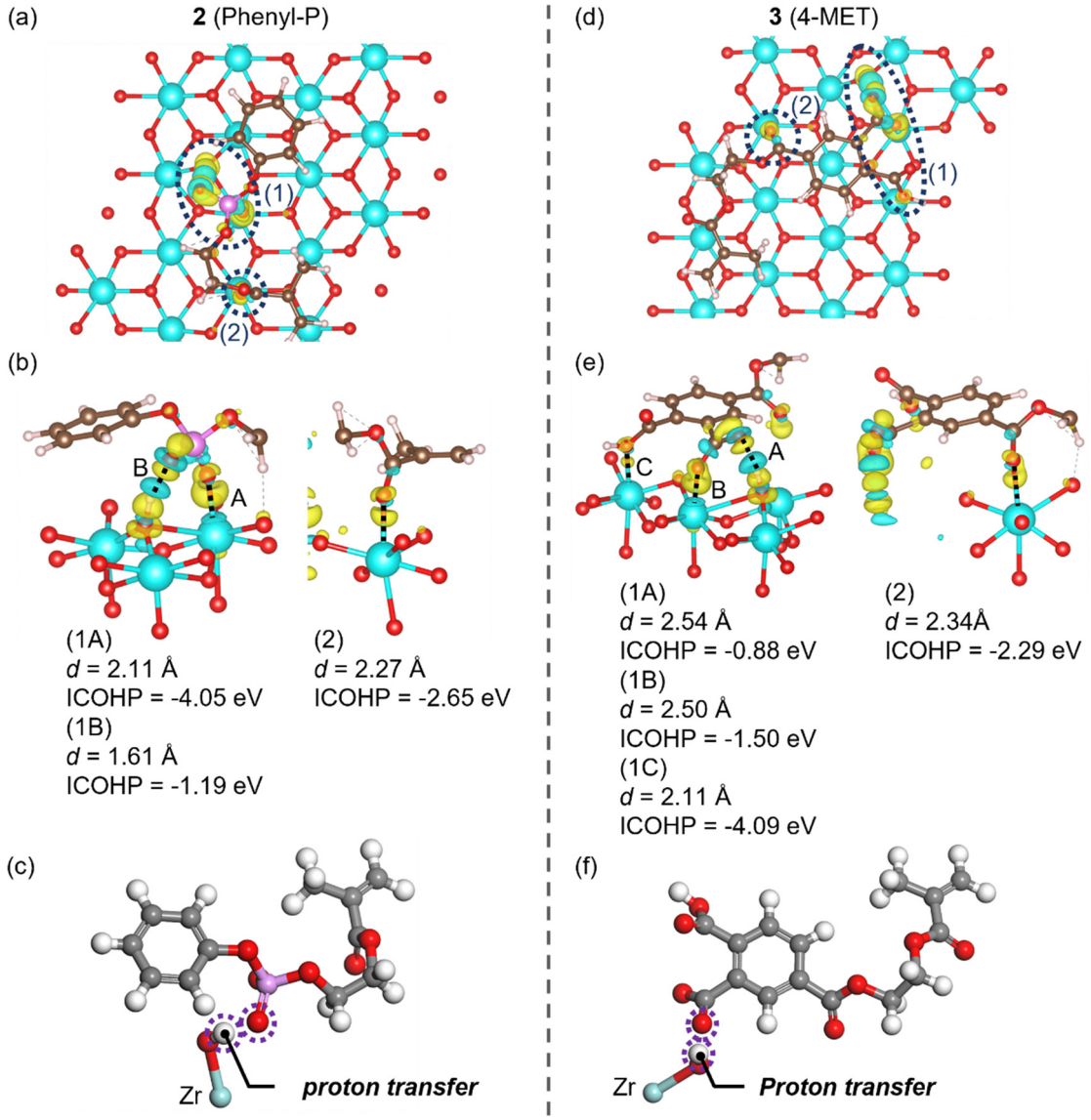

Fig. 8 (a) and (d) Charge density differences of (a) **2** and (d) **3**, respectively. (b) and (e) Enlarged views of (1) and (2) sites in (a) and (d), respectively. (c) and (f) Structures highlighting the proton transfer sites of Phenyl-P and 4-MET, respectively.

hydrogen bond formed with the hydrogen atom transferred to the surface. The interaction (2) is formed between the methacryloyl group and the zirconium atom, with an ICOHP value of −2.65 eV. In **3**, the two carboxylic acids strongly interacted with the surface and were labeled as (1A), (1B), and (1C). These ICOHP values were −0.88, −1.50, and −4.09 eV, respectively, and (1A) represented the hydrogen bond formed with the hydrogen atom transferred to the surface.

As described above, for all the three monomers **1**–**3**, barrierless proton transfer occurred from the acidic functional group to the surface, and multiple atomic pairs interacted between the acidic functional group and the surface *via* charge transfer. Notably, the absolute ICOHP value of the interaction between the oxygen atom of the acidic functional group and the zirconium atom, that is |ICOHP|, was large, indicating a strong interaction. In addition, the methacryloyl group contributed to interfacial interactions at all interfaces. The large DFT components of **1**–**3** shown in Fig. 6(a) are attributed to these interactions. These results were obtained by DFT calculation-based analysis. However, proton transfer and charge transfer interactions are difficult to handle using force-field calculations.

Charge density difference analysis was also applied to **1w**–**3w**. The charge-density differences for **1w** are shown in Fig. 9, and those for **2w** and **3w** are shown in Fig. 10. In Fig. 9(a), dotted lines (1)–(3) represent the sites where significant charge density changes occur in **1w**. Enlarged views from different angles are represented in Fig. 9(b). The isosurface value was set to 0.005 e $Å^{-3}$. The structures before and after the proton transfer, as determined by DFT optimization, are shown in Fig. 9(c). After proton transfer, the two oxygen atoms formed hydrogen bonds with the hydroxyl groups on the surface, as indicated by (1A), (1B), (1C), and (2). Their ICOHP values were

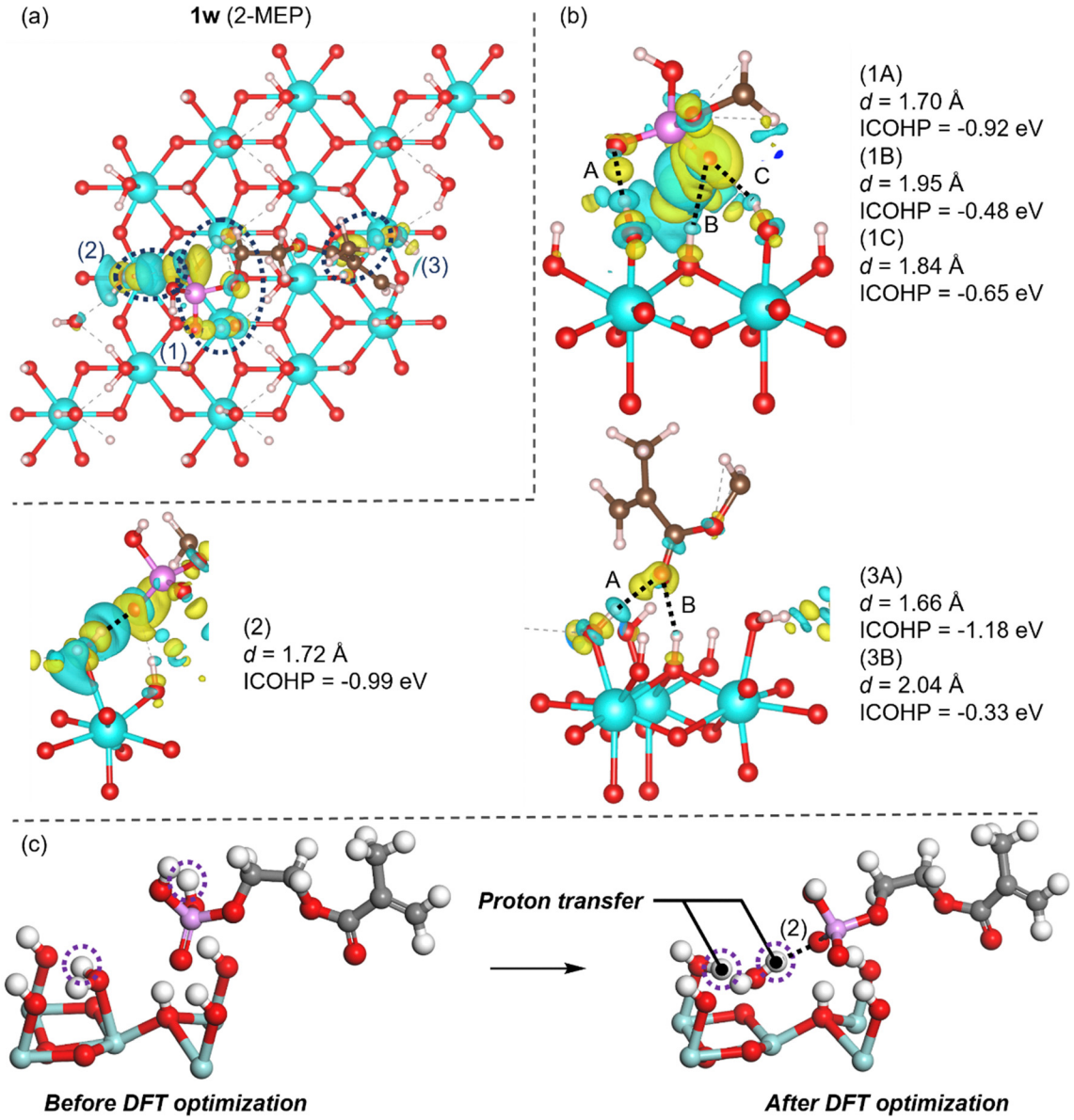

Fig. 9 (a) Charge density difference of **1w**. (b) Enlarged views of (1)–(3) sites. (c) Structural change of 2-MEP on the hydroxylated surface.

−0.92, −0.48, −0.65, and −0.99 eV, respectively. The interaction of the methacryloyl group with the surface was labeled as (3A) and (3B), and their ICOHP values were −1.18 and −0.33 eV. Notably, interaction (2), which exhibited the largest |ICOHP| value, corresponded to the hydrogen bonding between the hydrogen atom transferred to the surface and the oxygen atom of 2-MEP. This hydrogen bond formation is facilitated by two concerted proton transfers mechanism, as shown in Fig. 9(c). First, a hydrogen atom originally present in 2-MEP is transferred to a water molecule adsorbed on the surface. Then, a hydrogen atom from that water molecule is transferred to a hydroxyl group on the surface. Such a proton relay mechanism is rarely observed in adhesives like epoxy resins.[16,17,19,20,22–29,31] Through the charge density and COHP analysis of **1** and **1w**, it was found that chemical bond interactions involving significant charge transfer between 2-MEP and the surface were formed. These results are consistent with previous studies based on contact angle measurements[59] and spectroscopy,[12] which suggested that chemical bonds are formed between 10-MDP and zirconia surfaces.

In Fig. 10(a) and (c), the dotted lines (1), (2), and (3) indicate sites with significant charge density changes in **2w** and **3w**, respectively. Enlarged views from different angles are shown in Fig. 10(b) and (d). Notably, no proton transfer occurred from the adhesive monomer in **2w** and **3w**, unlike in **1w** and clean surfaces (**2** and **3**). For **2w**, the oxygen atom of the phenyl phosphate group formed interactions (1A) and (1B) with the hydroxy groups on the surface, and their corresponding ICOHP values were −0.88 and −0.14 eV, respectively. Additional interactions (2A) and (2B) were formed between the methacryloyl group and the surface with ICOHP values of −0.51 and −0.33 eV, respectively. In **3w**, the oxygen atom of the carboxy

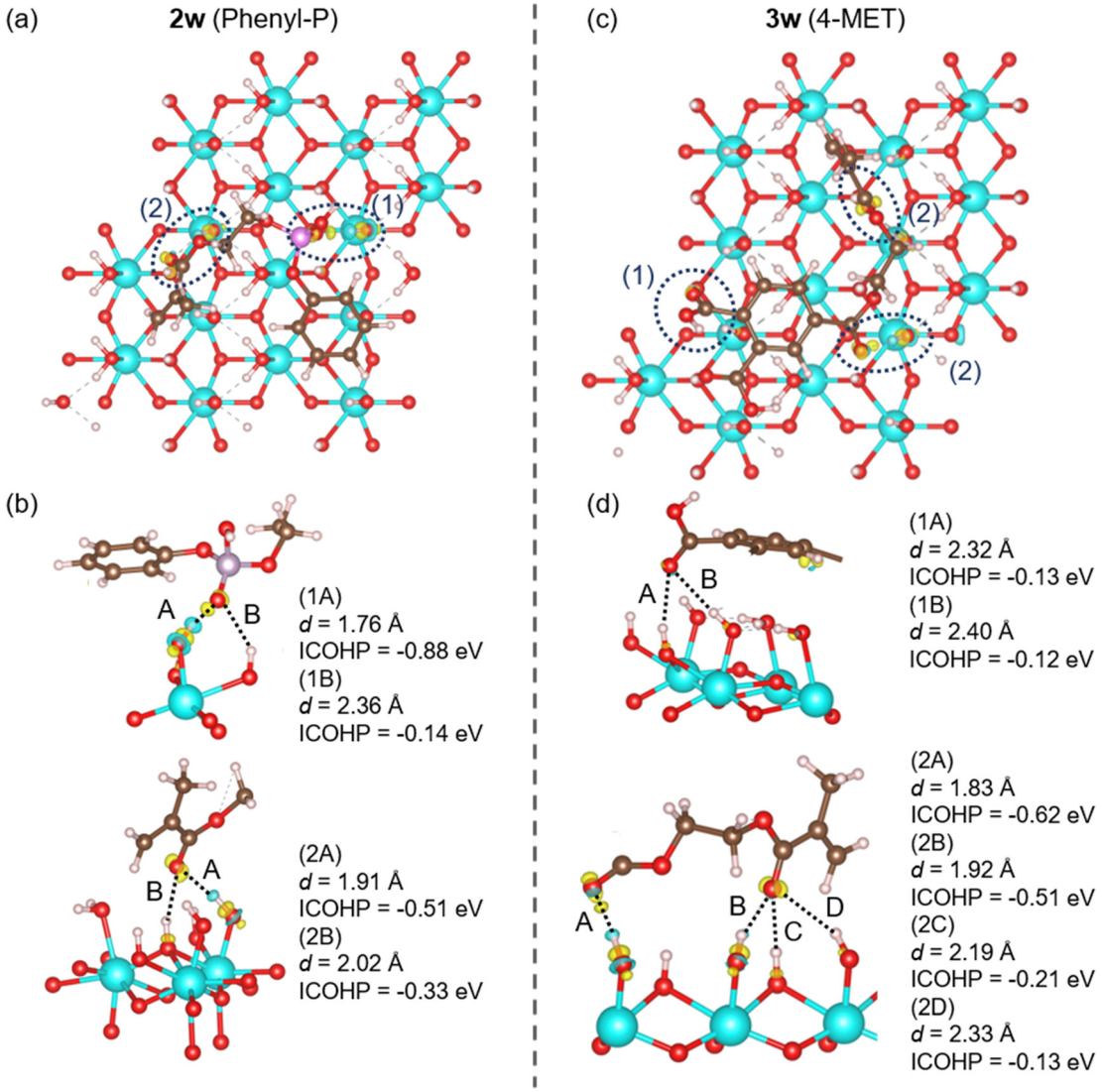

Fig. 10 (a) and (c) Charge-density differences of **2w** and **3w**. (b) and (d) Enlarged views of (1) and (2) sites in (a) and (c).

group formed interactions (1A) and (1B) with the hydroxy groups on the surface, with ICOHP values of −0.13 and −0.12 eV, respectively. Interactions (2A), (2B), (2C), and (2D) were formed between the methacryloyl group and surface, with the corresponding ICOHP values of −0.62, −0.51, −0.21, and −0.13 eV.

The ICOHP values of the interfacial interactions in **1w–3w** are classified by their origin from the acidic functional group and the methacryloyl group, respectively, as shown in Table 1. Among these, **1w** exhibited the highest total |ICOHP| values for the acidic functional group- and methacryloyl group-derived interactions. The total ICOHPI values for **1w**, **2w**, and **3w** were −4.55, −1.86, and −1.72 eV, respectively, and the order of these absolute values was **1w** > **2w** ≈ **3w**. This result indicated that the adhesive strength and DFT components of **1w** were larger

Table 1 ICOHP values for interactions derived from acidic functional and methacryloyl groups in **1w–3w** and their sums. Parentheses indicate the label number of the interaction with its ICOHP value

	ICOHP (eV)	
	Acidic functional group	Methacryloyl group
1w	(1A) −0.92, (1B) −0.48, (1C) −0.65, (2) −0.99	(2A) −1.18, (2B) −0.33
1w total	−3.04	−1.51
2w	(1A) −0.88, (1B) −0.14	(2A) −0.51, (2B) −0.33
2w total	−1.02	−0.84
3w	(1A) −0.13, (1B) −0.12	(2A) −0.62, (2B) −0.51, (2C) −0.21, (2D) −0.13
3w total	−0.25	−1.47

than those of **2w** and **3w**. This difference could be attributed to proton transfer to the surface, which was observed exclusively in **1w**. After proton transfer in **1w**, the oxygen atoms of the phosphate group served as hydrogen bonding acceptors on the surface, and four atomic pairs were involved in hydrogen bonding. The likelihood of proton transfer is based on the acidity of the adhesive monomer. The acidity of 10-MDP has been reported to be higher than that of Phenyl-P and 4-MET,[60,61] and 2-MEP may have a similar tendency. This finding indicated that proton transfer in **1w** occurred owing to the high acidity of 2-MEP. This high acidity was proposed to be the primary factor responsible for its superior adhesive strength. Notably, the total |ICOHP| value of the acidic functional group moiety of 4-MET (**3w**) was smaller than those of 2-MEP(**1w**) and Phenyl-P (**2w**). Considering that the methacryloyl group serves as a polymerization site of the monomer, the adhesive strength of **3w** might actually be even lower.

Finally, we discuss the theoretical estimation of adhesive strength performed in this study. The shear bond strength of 10-MDP measured experimentally in previous work was ~50 MPa at most,[12] which differs greatly from the adhesive strength estimated theoretically in this study. This discrepancy originates from the assumptions in the theoretical model. Specifically, the theoretical calculations assume the most stable conformation of the adhesive on the surface that the failure occurs at the adhesive–adherend interface, and an ideal surface without roughness and or defects. Quantitatively predicting adhesive strength beyond these model assumptions is important, but remains a challenging task. Nevertheless, the minimal models of this study enable efficiently capture the key molecular interactions at the interfaces and to provide qualitative insights into the relative adhesive affinities of different monomers and the origins of their interfacial interactions. These interfacial interactions are not easily observed directly through experiments. Verification through collaboration with experimental groups will be a topic for future work. No significant difference was observed in the adhesive performance between 2-MEP, Phenyl-P, and 4-MET for clean zirconia surfaces, but 2-MEP exhibited the highest adhesive strength for the hydroxylated surface. Among the adhesive monomers, 2-MEP demonstrated the highest acidity and induced proton transfer. Consequently, the oxygen atom served as a hydrogen bond acceptor after proton transfer, leading to an increase in adhesive strength. These findings provide valuable guidelines for the adhesion of zirconia dental materials.

4. Conclusions

To investigate the effects of the different functional groups of adhesive monomers on adhesion to zirconia dental materials, the adhesive interfaces between the three monomers (2-MEP, Phenyl-P, and 4-MET) and zirconia surfaces were analyzed using DFT calculations. No significant differences were observed on the clean surface; however, the adhesive strength of 2-MEP was the highest on the hydroxylated surface, corresponding to the wet environment, which was attributed to the DFT component. On comparing the adsorption structures of each adhesive monomer on the clean and hydroxylated surfaces, proton transfer was observed from the acidic functional group of all monomers to the clean surface, whereas only 2-MEP caused proton transfer on the hydroxylated surface.

By applying charge density difference analysis, large changes in charge density were observed on all surfaces, indicating that interactions involving charge transfer played an important role in adhesion to zirconia. By applying COHP analysis to these interfacial interactions, the phosphate group of 2-MEP was observed to form multiple interactions with the hydroxylated surface, with the oxygen atom serving as the hydrogen bond acceptor to the hydroxyl groups on the surface after proton transfer. This proton transfer was attributed to the high acidity of 2-MEP.

The insights into the high adhesive performance of 2-MEP can contribute to the selection and improvement of active ingredients in commercially available zirconia bonding kits. The adhesion mechanism involving charge transfer interactions with the zirconia surface, initiated by proton transfer from the phosphoric acid group, supports the effectiveness of 10-MDP-type monomers,[12] which are widely used in clinical practice. This charge transfer interaction can be enhanced with increasing acidity of the functional group in adhesive monomers, providing a valuable design principle for future monomer development.

Conflicts of interest

There are no conflicts to declare.

Data availability

Data will be made available upon request.

Acknowledgements

This work was supported by the KAKENHI grant (number JP25K18002) from the Japan Society for the Promotion of Science (JSPS), the Iketani Science and Technology Foundation (ISTF), the Foundation of Amano Institute of Technology, the Tokuyama Science Foundation, the Takahashi Industrial and Economic Research Foundation, and the Toshiaki Ogasawara Memorial Foundation. The computations in this work were primarily performed using computer facilities at the Research Institute for Information Technology, Kyushu University, the Supercomputer Center, the Institute for Solid State Physics, the University of Tokyo, and Research Center for Computational Science, Okazaki, Japan (Project 25-IMS-C141).

References

1 J. Perdigão, E. Araujo, R. Q. Ramos, G. Gomes and L. J. Pizzolotto, *Esthet. Restor. Dent*, 2021, **33**, 51–68.

2 H. Wang, M. N. Aboushelib and A. Feilzer, *J. Dent. Mater.*, 2008, **24**, 633–638.
3 C. Gross, T. Bergfeldt, T. Fretwurst, R. Rothweiler, K. Nelson and A. Stricker, *J. Mech. Behav. Biomed. Mater.*, 2020, **107**, 103759.
4 N. Cionca, D. Hashim and A. Mombelli, *Periodontol*, 2000, **73**, 241–258.
5 B. Kim, Y. Zhang, M. Pines and V. P. Thompson, *J. Dent. Res.*, 2007, **86**, 142–146.
6 I. Denry and J. R. Kelly, *Dent. Mater.*, 2008, **24**, 299–307.
7 R. Giordano and E. A. McLaren, *Compend. Contin. Educ. Dent.*, 2010, **31**, 682–688.
8 B. Stawarczyk, M. Özcan, L. Hallmann, A. Ender, A. Mehl and C. H. F. Hämmerlet, *Clin. Oral Invest*, 2012, **17**, 269–274.
9 S. Inoue, M. A. Vargas, Y. Abe, Y. Yoshida, P. Lambrechts, G. Vanherle, H. Sano and B. Van Meerbeek, *J. Adhes. Dent.*, 2001, **3**, 237–246.
10 S. Inoue, K. Koshiro, Y. Yoshida, J. De Munck, K. Nagakane, K. Suzuki, H. Sano and B. Van Meerbeek, *J. Dent. Res.*, 2005, **84**, 1160–1164.
11 Y. Yoshida, K. Nagakane, R. Fukuda, Y. Nakayama, M. Ozaki, H. Shintani, S. Inoue, Y. Tagawa, K. Suzuki, J. D. Munck and B. V. Meerbeek, *J. Dent. Res.*, 2004, **83**, 454–458.
12 N. Nagaoka, K. Yoshihara, V. P. Feitosa, Y. Tamada, M. Irie, Y. Yoshida, B. V. Meerbeek and S. Hayakawa, *Sci. Rep.*, 2017, **7**, 45563.
13 Y. Chen, Z. Lu, M. Qian, H. Zhang, C. Chen, H. Xie and F. R. Tay, *Dent. Mater.*, 2017, **33**, e415–e427.
14 R. S. Calamita, A. A. D. Oliveira, G. G. Pizzanelli, M. V. O. Salvador, A. M. M. Mesquita, V. G. A. Pecorari and A. F. Lima, *Dent. Mater.*, 2023, **39**, 665–668.
15 Y. Morimitsu, H. Matsuno, Y. Oda, S. Yamamoto and K. Tanaka, *Sci. Adv.*, 2022, **8**, 6349.
16 S. Ogata and Y. Takahashi, *J. Phys. Chem. C*, 2016, **120**, 13630–13637.
17 G. Bahlakeh, M. Ghaffari, M. R. Saeb, B. Ramezanzadeh, F. De Proft and H. Terryn, *J. Phys. Chem. C*, 2016, **120**, 11014–11026.
18 K. Min, A. R. Rammohan, H. S. Lee, J. Shin, S. H. Lee, S. Goyal, H. Park, J. C. Mauro, R. Stewart, V. Botu, H. Kim and E. Cho, *Sci. Rep.*, 2017, **7**, 10475.
19 G. Bahlakeh and B. Ramezanzadeh, *ACS Appl. Mater. Interfaces*, 2017, **9**, 17536–17551.
20 S. Ogata and M. Uranagase, *J. Phys. Chem. C*, 2018, **122**, 17748–17755.
21 D. J. Eyckens, F. Stojcevski, A. Hendlmeier, D. J. Randall, D. J. Hayne, M. K. Stanfield, B. Newman, F. Vukovic, T. R. Walsh and L. C. Henderson, *J. Mater. Chem. A*, 2021, **9**, 26528–26572.
22 Y. Sumiya, Y. Tsuji and K. Yoshizawa, *Phys. Chem. Chem. Phys.*, 2022, **24**, 27289–27301.
23 Y. Sumiya, Y. Tsuji and K. Yoshizawa, *ACS Omega*, 2022, **7**, 17393–17400.
24 T. Uwabe, Y. Sumiya, Y. Tsuji, S. Nakamura and K. Yoshizawa, *Langmuir*, 2023, **39**, 18537–18547.
25 S. Chai, J. Liu, D. Hou and P. Wang, *RSC Adv.*, 2023, **13**, 30915–30924.
26 S. Ogata and M. Uranagase, *J. Phys. Chem. B*, 2023, **127**, 2629–2638.
27 A. Shrestha, Y. Sumiya, K. Okazawa, T. Uwabe and K. Yoshizawa, *Langmuir*, 2023, **39**, 5514–5526.
28 K. Hagita, T. Miyata and H. Jinnai, *Langmuir*, 2023, **39**, 7063–7078.
29 A. Shrestha, Y. Sumiya, K. Okazawa, Y. Tsuji and K. Yoshizawa, *Langmuir*, 2024, **40**, 21573–21586.
30 K. Kikkawa, Y. Sumiya, K. Okazawa, K. Yoshizawa, Y. Itoh and T. Aida, *J. Am. Chem. Soc.*, 2024, **146**, 21168–21175.
31 Y. Sumiya, R. Kaji and K. Yoshizawa, *Chem. Phys. Lett.*, 2024, **847**, 141370.
32 M. Nakatani, S. Fukamachi, P. Solis-Fernandez, S. Honda, K. Kawahara, Y. Tsuji, Y. Sumiya, M. Kuroki, K. Li, Q. Liu, Y.-C. Lin, A. Uchida, S. Oyama, H. G. Ji, K. Okada, K. Suenaga, Y. Kawano, K. Yoshizawa, A. Yasui and H. Ago, *Nat. Electron.*, 2024, **7**, 119–130.
33 Y. Sumiya and T. Uwabe, *J. Mater. Chem. B*, 2025, **13**, 5095–5108.
34 T. Aoyama, N. Kurata, K. Hirota and O. Yamaguchi, *J. Am. Ceram. Soc.*, 1995, **78**, 3163–3164.
35 A. Hofman, S. J. Clark, M. Oppel and I. Hahndorf, *Phys. Chem. Chem. Phys.*, 2002, **4**, 3500–3508.
36 R. Anez, A. Sierralta and P. Sautet, *J. Phys. Chem. C*, 2007, **111**, 8314–8320.
37 K. Rabel, J. Nold, D. Pehlke, J. Shen, A. Abram, A. Kocjan, S. Witkowski and R. J. Kohal, *J. Mech. Behav. Biomed. Mater.*, 2022, **135**, 105456.
38 G. Kresse and J. Hafner, *Phys. Rev. B: Condens. Matter Mater. Phys.*, 1993, **47**, 558–561.
39 G. Kresse and J. Hafner, *Phys. Rev. B: Condens. Matter Mater. Phys.*, 1994, **49**, 14251–14269.
40 G. Kresse and J. Furthmüller, *Comput. Mater. Sci.*, 1996, **6**, 15–50.
41 J. P. Perdew and K. Burke, *Phys. Rev. Lett.*, 1996, **77**, 3865–3868.
42 S. Grimme, S. Ehrlich and L. Goerigk, *J. Comput. Chem.*, 2011, **32**, 1456–1465.
43 G. Kresse and D. Joubert, *Phys. Rev. B: Condens. Matter Mater. Phys.*, 1999, **59**, 1758–1775.
44 B. Adolph, J. Furthmüller and F. Beckstedt, *Phys. Rev. B: Condens. Matter Mater. Phys.*, 2001, **63**, 125108.
45 BIOVIA Materials Studio. Materials studio 2024; Dassault Systèmes: San Diego, 2024.
46 B. Leimkuhler, E. Noorizadeh and F. A. Theil, *J. Stat. Phys.*, 2009, **135**, 261–277.
47 S. L. Mayo, B. D. Olafson and W. Goddard, *J. Phys. Chem.*, 1990, **94**, 8897–8909.
48 T. Kosmac, C. Oblak, P. Jevnikar, N. Funduk and L. Marion, *Dent. Mater.*, 1999, **15**, 426–433.
49 L. M. Schabbach, B. C. dos Santos, L. S. De Bortoli, D. Fabris, M. C. Fredel and B. Henriques, *Dent. Mater.*, 2023, **39**, 807–819.
50 C. Higuchi, H. Tanaka and K. Yoshizawa, *J. Comput. Chem.*, 2019, **40**, 164–171.

51 S. A. Veldhuis, P. Brinks and J. E. ten Elshof, *Thin Solid Films*, 2015, **589**, 503–507.
52 J. Lahiri, A. Mayernick, S. L. Morrow, B. E. Koel, A. C. T. van Duin, M. J. Janik and M. Batzill, *J. Phys. Chem. C*, 2010, **114**, 5990–5996.
53 A. Abbasi, *RSC Adv.*, 2019, **9**, 16069–16082.
54 S. Steinberg and R. Dronskowski, *Crystals*, 2018, **8**, 225.
55 S. Maintz, V. L. Deringer, A. L. Tchougréeff and R. Dronskowski, *J. Comput. Chem.*, 2016, **37**, 1030–1035.
56 R. Dronskowski and P. E. Blöchl, *J. Phys. Chem.*, 1993, **97**, 8617–8624.
57 V. L. Deringer, A. L. Tchougréeff and R. Dronskowski, *J. Phys. Chem. A*, 2011, **115**, 5461–5466.
58 K. Momma and F. Izumi, *J. Appl. Crystllogr.*, 2011, **44**, 1272–1276.
59 L. Chen, B. I. Suh, D. Brown and X. Chen, *Am. J. Dent.*, 2012, **25**, 103–108.
60 M. Ogata, N. Harada, S. Yamaguchi, M. Nakajima, P. N. R. Pereira and J. Tagami, *Oper. Dent.*, 2001, **26**, 375–382.
61 K. Yoshihara, Y. Yoshida, S. Hayakawa, N. Nagaoka, M. Irie, T. Ogawa, K. L. V. Landuyt, A. Osaka, K. Suzuki, S. Minagi and B. V. Meerbeek, *Acta Biomater.*, 2011, **7**, 3187–3195.

